

# First Observational Tests of Eternal Inflation

Stephen M. Feeney,<sup>1,\*</sup> Matthew C. Johnson,<sup>2,3,†</sup> Daniel J. Mortlock,<sup>4,‡</sup> and Hiranya V. Peiris<sup>1,5,§</sup>

<sup>1</sup>*Department of Physics and Astronomy, University College London, London WC1E 6BT, U.K.*

<sup>2</sup>*Perimeter Institute for Theoretical Physics, Waterloo, Ontario N2L 2Y5, Canada*

<sup>3</sup>*California Institute of Technology, Pasadena, CA 91125, USA*

<sup>4</sup>*Astrophysics Group, Imperial College London, Blackett Laboratory, Prince Consort Road, London, SW7 2AZ, U.K.*

<sup>5</sup>*Institute of Astronomy and Kavli Institute for Cosmology,  
University of Cambridge, Cambridge CB3 0HA, U.K.*

(Dated: December 10, 2010)

The eternal inflation scenario predicts that our observable universe resides inside a single bubble embedded in a vast multiverse, the majority of which is still undergoing super-accelerated expansion. Many of the theories giving rise to eternal inflation predict that we have causal access to collisions with other bubble universes, opening up the possibility that observational cosmology can probe the dynamics of eternal inflation. We present the first observational search for the effects of bubble collisions, using cosmic microwave background data from the WMAP satellite. Using a modular algorithm that is designed to avoid *a posteriori* selection effects, we find four features on the CMB sky that are consistent with being bubble collisions. If this evidence is corroborated by upcoming data from the *Planck* satellite, we will be able to gain insight into the possible existence of the multiverse.

**Introduction:** The inflationary paradigm has been very successful at explaining the initial conditions giving rise to our observable universe. Turning back the clock even further, considering the initial conditions for inflation itself leads to the surprising possibility that our observable universe might only be a tiny piece of a vast multiverse, the majority of which is still undergoing accelerated expansion. In this scenario, known as eternal inflation (for a review, see e.g. Ref. [1]), our observable universe resides inside a single bubble nucleated out of a false vacuum de Sitter space. The rate of bubble formation is outpaced by the accelerated expansion of the inflating false vacuum, and therefore inflation does not end everywhere.

Eternal inflation is ubiquitous in theories with extra dimensions (string theory being the primary example) and positive vacuum energy, and therefore constitutes a well-motivated scenario for the early universe that one would like to confront with observation. Testing this scenario is extremely difficult since eternal inflation is a *pre-inflationary* epoch, and any signals from outside of our bubble would naively appear to be stretched to unobservable super-horizon scales. While this is in general true, one exciting prospect for probing this epoch lies in the observation of the collisions between vacuum bubbles. These collisions produce inhomogeneities in the inner-bubble cosmology, raising the possibility that their effects are imprinted in the cosmic microwave background (CMB) [2]. In this paper we describe a set of algorithms designed to look for bubble collisions in the CMB, and ap-

ply them to the *Wilkinson Microwave Anisotropy Probe* (WMAP) 7-year data [3].

Recent work (see the review Ref. [4] and references therein) has established that: the presence of bubble collisions can be compatible with our observed cosmology; in some models, collisions are likely to be within our past light cone; and collisions can leave observable signatures. The degree to which these criteria for observing bubble collisions are satisfied is highly dependent on: the scalar field potential(s) that drive eternal inflation (which controls the rate of bubble formation); the duration of inflation inside our bubble (the more inflation the more dilute the signal); and the particular realization of the CMB sky and bubble collisions we might observe (i.e. even a clear signal could be obscured by foregrounds). Although there is ample motivation to consider the eternal inflation scenario, a concrete model (of, say, the string theory landscape) providing all of these details does not currently exist.

Nevertheless, bubble collisions produce a rather generic set of signatures that we target in our analysis:

**Azimuthal symmetry:** A collision leaves an imprint on the CMB sky that has azimuthal symmetry. This is a consequence of the SO(2,1) symmetry of the spacetime describing the collision of two vacuum bubbles.

**Causal boundary:** The surface of last scattering can only be affected inside the future light cone of a collision event. The intersection of our past light cone, the future light cone of a collision, and the surface of last scattering is a ring. The observed temperature of the CMB need not be continuous across this boundary.

**Long-wavelength modulation inside the causal boundary:** A bubble collision is a pre-inflationary relic. The effects of a collision have been stretched by inflation, and induce an overall modulation of the CMB temperature anisotropies [5].

\* stephen.feeney.09@ucl.ac.uk

† mjohnson@perimeterinstitute.ca

‡ d.mortlock@imperial.ac.uk

§ h.peiris@ucl.ac.uk

At the time of last scattering, the signal is long-wavelength, has approximate planar symmetry (from the observed smallness of the normalized curvature density,  $\Omega_k$ ), and has a causal boundary, implying that if a bubble collision was centred at the north pole, the observed temperature fluctuation caused by the collision would take the form:

$$\frac{\delta T}{T} = [c_0 + c_1 \cos \theta + \mathcal{O}(\cos^2 \theta)] \Theta(\theta_{\text{crit}} - \theta), \quad (1)$$

where the  $c_i$  are constants and  $\Theta(\theta_{\text{crit}} - \theta)$  is a step function at the causal boundary  $\theta_{\text{crit}}$ . An identical result is obtained using a test-field to approximate the behaviour of the inflaton in the presence of a collision [5]. For a long-wavelength fluctuation, we keep only the first two terms in Eq. 1, and write the constants  $c_0$  and  $c_1$  in terms of  $z_0$ , the amplitude of the temperature modulation at the centre of the collision, and  $z_{\text{crit}}$ , the discontinuity of the temperature at the causal boundary:

$$c_0 = \frac{z_{\text{crit}} - z_0 \cos \theta_{\text{crit}}}{1 - \cos \theta_{\text{crit}}}, \quad c_1 = \frac{z_0 - z_{\text{crit}}}{1 - \cos \theta_{\text{crit}}}. \quad (2)$$

Including the location of the collision centre,  $\{\theta_0, \phi_0\}$ , a collision can be described by five parameters:  $\{z_0, z_{\text{crit}}, \theta_{\text{crit}}, \theta_0, \phi_0\}$ . An example of the CMB temperature modulation produced by a bubble collision is shown in the top left of Fig. 1.

**Data and simulations:** Our analysis pipeline is general, but it is important to calibrate each step using simulations of the particular data-set under consideration. WMAP has measured the intensity and polarization of the microwave sky in five frequency bands. The resolution of the instrument in each band is limited by the detectors' beams, and is highest at  $0.22^\circ$  in the 94 GHz W band. We perform our analysis on the foreground-subtracted W-band WMAP temperature map, as this combines the highest resolution full-sky data currently available with the least foreground contamination. To minimize the effects of the residual foregrounds we cut the sky with the conservative KQ75 mask, leaving 70.6% of the sky unmasked.

To calibrate detection thresholds in our analysis pipeline and quantify the expected false detection rate, we use an end-to-end simulation of the W-band channel of the WMAP instrument, provided by the WMAP Science Team. This is generated from a simulated time ordered data stream (containing Galactic foregrounds, CMB fluctuations, realistic instrumental noise, finite beam size, and other instrumental effects) which is processed using the same pipeline as applied to the actual data.

To determine the sensitivity of our analysis pipeline to bubble collisions, we generate simulated temperature maps containing CMB fluctuations, a bubble collision, instrumental noise, and smoothing to emulate the W-band beam. We consider collisions with  $\theta_{\text{crit}} = 5^\circ, 10^\circ, 25^\circ$

and choose centres in a high and low-noise region of the sky such that the signal remains in each case significantly outside of the KQ75 7-year mask. For each  $\theta_{\text{crit}}$  and location, we generate 35 simulated collisions logarithmically spaced between the parameter ranges  $10^{-6} \leq z_{\text{crit}} \leq 10^{-4}$  and  $-10^{-4} \leq z_0 \leq -10^{-6}$ . The response of our pipeline depends only on the absolute value of  $z_0$  and  $z_{\text{crit}}$ , so the choice of sign for  $z_0$  and  $z_{\text{crit}}$  is arbitrary. We repeat this process for three realizations of the background CMB fluctuations, yielding a total of 210 simulated sky maps for each of the three collision sizes.

**Method:** Our analysis pipeline is fully automated, and calibrated using realistic simulations before being applied to the real data. It is critical to minimize human intervention when anomaly hunting in the CMB. As the large body of literature on the subject shows, it is rather easy to find all sorts of statistically unlikely properties in a large dataset like the CMB due to a *posteriori* selection effects [6]: the human eye is good at finding non-existent patterns in “random” data.

An optimal search algorithm would be to perform Bayesian model selection on the full CMB sky for an arbitrary number of modulations of the form Eq. 1. However, at full WMAP resolution, this is computationally impossible. We therefore develop a three-step analysis pipeline (schematically depicted in Fig. 1) that first segments the sky into regions containing the most interesting features, and then processes each segment to search for signals specific to a bubble collision:

1. A “blob-detection” step using needlets [7] (a type of wavelet) is used to identify significant features in the temperature map and determine their approximate location and angular size. This step targets the azimuthal symmetry and localization of a bubble collision.
2. An edge detection algorithm is then applied to search for circular temperature discontinuities within the most significant regions. This step targets the causal boundary associated with a bubble collision.
3. A pixel-based Bayesian parameter estimation and model selection analysis is performed on the regions of sky highlighted by the previous steps. This step targets the specific form of the temperature modulation given by Eq. 1.

**Blob detection:** To identify the most promising candidate signals in a temperature map, we perform a suite of spherical needlet transforms:

$$\beta_{jk} = \sum_{\ell} b_{\ell}(j) \sum_{m=-\ell}^{\ell} a_{\ell m} Y_{\ell m}(\xi_{jk}) \quad (3)$$

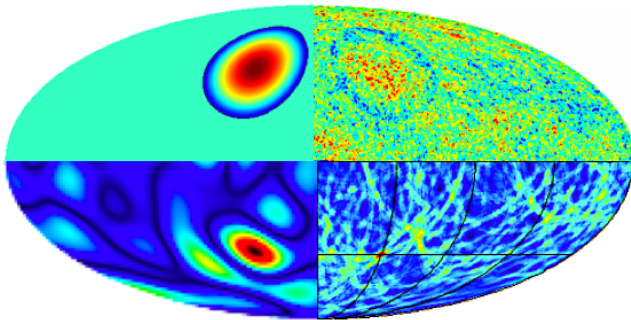


FIG. 1. The signatures of a bubble collision at various stages in our analysis pipeline. A collision (top left) induces a temperature modulation in the CMB temperature map (top right). The “blob” associated with the collision is identified by a large needlet response (bottom left), and the presence of an edge is determined by a large response from the edge detection algorithm (bottom right).

( $j$  = frequency,  $k$  = HEALPix pixel [8]), where  $Y_{\ell m}$  are the spherical harmonics,  $a_{\ell m}$  are the spherical harmonic coefficients of an input map, and  $b_{\ell}(j)$  is a frequency-dependent filter function determining the needlet shape. Two classes of needlet shapes (“standard” [7] and “Mexican” [9]) are used to ensure that we are sensitive to a wide variety of modulations. We optimize the needlet response to a variety of collision templates by adjusting the band-width of  $b_{\ell}(j)$ . Optimal unbiased maximum-likelihood estimators of the  $a_{\ell m}$ s [10] are used at low- $\ell$  to partially off-set the effects of the mask on low-frequency needlet coefficients; cut-sky  $a_{\ell m}$ s are used at larger  $\ell$ .

In the lower left quadrant of Fig. 1 we plot  $\beta_{jk}$  for fixed  $j$  at each pixel  $k$  obtained for a simulated map containing a collision. The needlet coefficients clearly take their largest value in the vicinity of the collision. The strength of this response is needlet frequency dependent; therefore finding the frequency of maximum response yields information about the angular scale of the collision.

For a purely Gaussian uncut CMB sky, the average needlet coefficient is zero for all  $j, k$ , and the variance of the needlet coefficients for fixed  $j$  at each pixel  $k$  is identical and directly related to the scalar temperature power spectrum. Cutting the sky introduces a  $j$ - and  $k$ -dependent bias, and we determine the significance of a needlet coefficient by:

$$S_{jk} = \frac{|\beta_{jk} - \langle \beta_{jk} \rangle_{\text{gauss, cut}}|}{\sqrt{\langle \beta_{jk}^2 \rangle_{\text{gauss, cut}}}} \quad (4)$$

where the average  $\langle \beta_{jk} \rangle_{\text{gauss, cut}}$  and variance  $\langle \beta_{jk}^2 \rangle_{\text{gauss, cut}}$  are calculated at each pixel from the needlet coefficients of 3000 collision-free Gaussian CMB realizations with the 7-year KQ75 sky cut applied.

Because there are many independent needlet coefficients in any given realization, there are features of fairly large significance even in a purely Gaussian map. To

minimize the number of such false detections, we use the needlet response to the end-to-end simulation to define a set of frequency- and shape-dependent detection thresholds (ranging from  $3 \leq S_{jk} \leq 3.75$ ). A total of 10 false detections are found in the end-to-end simulation using these thresholds. Regions with 5 or more pixels whose needlet coefficients exceed these thresholds are grouped into “blobs”. To take full advantage of the angular scale information in the needlet coefficients, we then build a lookup table consisting of the range of  $\theta_{\text{crit}}$  over which each needlet frequency yields the maximum response.

We have tested the performance of the blob detection step using the full set of simulated collisions. The results are presented in Fig. 2 (left panel) as “exclusion” and “sensitivity” regions of the  $\{z_0, z_{\text{crit}}\}$  parameter space for  $\theta_{\text{crit}} = 10^\circ$  (the  $\theta_{\text{crit}} = 5^\circ$  and  $25^\circ$  results are nearly identical). If we detect all 6 simulated bubble collisions at a given point  $\{z_0, z_{\text{crit}}\}$  of parameter space, then a non-detection in the real data would imply we can exclude such collisions; if we detect a collision for a subset of the simulations, then we are sensitive to collisions in this region of parameter space.

**Edge detection:** The second step of the pipeline tests features highlighted by the blob detection stage for circular temperature discontinuities (controlled by  $z_{\text{crit}}$ ), a smoking gun signature of bubble collisions. To generate a set of candidate edges, we have developed an implementation of the Canny algorithm [11] for the HEALPix pixelization scheme. In this algorithm, the gradient of an image is generated, smoothed to reduce the effects of pixel noise, and thinned into local maxima, the strongest of which are stitched together into edges.

An adaptation of the Circular Hough Transform (CHT) algorithm [12] is then applied to evaluate if these candidate edges fall on circles of varying centre and angular radius. If a map of the “CHT score” (i.e. the normalized hit count)  $N_{\text{hits}}/\theta_{\text{crit}}$  is sharply peaked at a specific angular scale  $\theta_{\text{crit}}$ , then this is indicative of a circular edge of this radius centered on the peak. In the example in the bottom right quadrant of Fig. 1, the peak in the CHT score at the true centre of the collision shows an unambiguously detected edge. We have verified that none of the false detections flagged in the end-to-end simulations have a significant peak.

The sensitivity and exclusion regions from the edge-detection step are shown in Fig. 2 (right panel) for the  $10^\circ$  simulated collisions. For the  $5^\circ$  collisions, the proliferation of degree-sized features in the background CMB affects performance, yielding a similar sensitivity region, but a much smaller exclusion region (including only  $z_0 \gtrsim 10^{-4}$  and  $z_{\text{crit}} \lesssim -10^{-4}$ ). The exclusion and sensitivity regions for the  $25^\circ$  collisions are, again, nearly identical to those for the  $10^\circ$  collisions.

Based on these results, the first two steps of our pipeline can detect bubble collisions with central modulations  $|z_0| \gtrsim 3 \times 10^{-5}$  and causal edges  $|z_{\text{crit}}| \gtrsim 3 \times 10^{-5}$

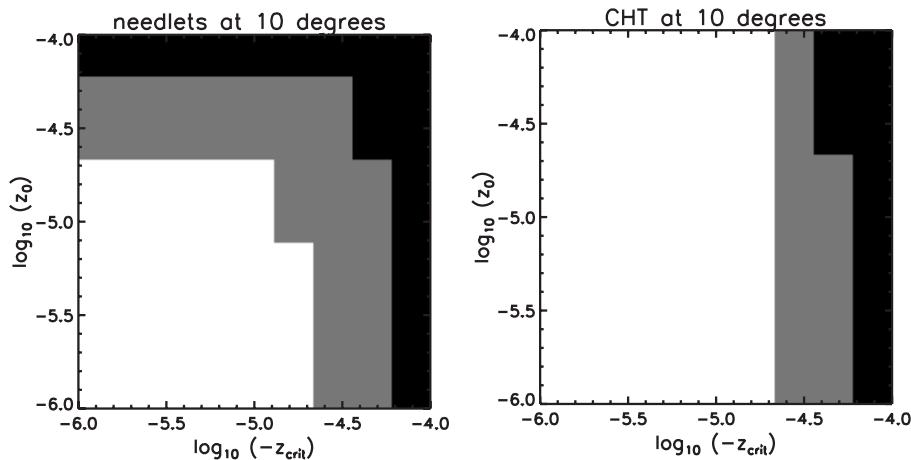


FIG. 2. Exclusion (black) and sensitivity (grey) regions for the needlet (left) and edge-detection (right) steps of the analysis pipeline applied to a set of  $\theta_{\text{crit}} = 10^\circ$  simulated bubble collisions. Collisions in the exclusion region would be definitively detected as long as they were not significantly masked. Collisions in the sensitivity region could be found if they were in a favorable location of the sky (i.e. low noise, or a region with a specific realization of CMB fluctuations which did not obscure the causal edge).

at  $\theta_{\text{crit}} \gtrsim 5^\circ$ .

**Bayesian model selection:** In order to verify whether a significant feature is well-modelled as a bubble collision, we perform Bayesian model selection for the bubble template Eq. 1, denoted  $M_b$ , versus the standard model given by pure CMB and WMAP instrumental effects, denoted  $M_0$ . From Bayes' Theorem (e.g. Ref. [13]), the relative probability of these two models given data  $\mathbf{d}$  is

$$\frac{P(M_b|\mathbf{d})}{P(M_0|\mathbf{d})} = \frac{P(M_b)\mathcal{Z}_b}{P(M_0)\mathcal{Z}_0}, \quad (5)$$

where  $P(M_b)/P(M_0)$  is the *a priori* probability ratio of the two models (which we set to 1), and the model-averaged likelihood (or *evidence*)  $\mathcal{Z}$  is given by

$$\mathcal{Z} = \int \mathcal{L}(\mathbf{d}|\Theta)\pi(\Theta)d^n\Theta. \quad (6)$$

Here,  $\mathcal{L}(\mathbf{d}|\Theta)$  is the likelihood of the data given the  $n$  model parameters  $\Theta$ , and  $\pi(\Theta)$  are priors on these parameters. The evidence ratio  $\rho = \mathcal{Z}_b/\mathcal{Z}_0$  of the two models indicates which better describes the data.

We use the nested sampler Multinest [14] to calculate the evidence in favour of bubble collisions  $\mathcal{Z}_b$ . The (exact) pixel-space likelihood is  $\mathcal{L} \propto \exp[-(\mathbf{D} - \mathbf{T})\mathbf{C}^{-1}(\mathbf{D} - \mathbf{T})/2]$ . Here  $\mathbf{D}$  is the data in the vicinity of the candidate event (computationally limited to patches of radius  $\lesssim 11^\circ$ ),  $\mathbf{T}$  is the temperature modulation caused by the collision, and  $\mathbf{C}$  is the pixel-pixel covariance matrix, including cosmic variance given by the best fit  $C_\ell$  as well as the W-band noise and beam from the WMAP 7-year data release. The collision-free model  $M_0$  is a special case of  $M_b$  whose prior is a delta function picking out the parameter combinations yielding zero-amplitude collisions.

Its evidence  $\mathcal{Z}_0$  can therefore be calculated by a single evaluation of the likelihood  $\mathcal{L}$  with  $\mathbf{T} = \mathbf{0}$ .

We use uniform priors throughout, restricting  $\{\theta_0, \phi_0\}$  to lie in the pixels passing the needlet significance threshold, a range of  $\theta_{\text{crit}}$  defined by the needlet response to each blob, and  $z_0$  and  $z_{\text{crit}}$  in the range  $-10^{-4}$  to  $10^{-4}$  imposed by the observed CMB. The evidence ratios for false detections in the end-to-end simulation increase with the needlet frequency at which the detection is made. The evidence ratios for features fit by  $\theta_{\text{crit}} \gtrsim 5^\circ$  were bounded by  $\ln \rho < 2.6$ , while the evidence ratio for smaller features could be as large as  $\ln \rho \sim 5.5$ . The evidence ratio obtained for a collision in the exclusion region is  $\ln \rho \sim 130$ . We find that collisions with a causal edge in the sensitivity region yield evidence ratios  $\ln \rho \sim 5.0$ , while collisions with similar  $z_0$ , but  $z_{\text{crit}} \sim 0$ , yield evidence ratios  $\ln \rho \sim 3$ ; the presence of an edge greatly increases the potential significance of a detection. In summary, using Bayesian model selection we can definitively detect all bubble collisions in the needlet exclusion region of parameter space, and have the ability to make detections in the sensitivity region of parameter space if the collision occurs in a favorable location.

**Analysis of the WMAP 7-year data:** Applying the needlet step of our pipeline to the WMAP 7-year W-band temperature map with the KQ75 mask, we find 15 significant features, 11 of which are sufficiently distant from the mask to merit further examination. The number of features and their significance range is fairly consistent with the end-to-end simulation (we find needlet significances ranging from  $3.37 \leq S_{jk} \leq 4.58$ ). The edge-detection results are also consistent with those from the end-to-end simulation, with no clear peaks in the CHT score for any of the significant features. We can therefore

rule out the presence of any large angular scale bubble collisions with values of  $\{z_0, z_{\text{crit}}\}$  in the CHT exclusion region of Fig. 2.

Of the 11 significant features, 4 have evidence ratios exceeding the maximum ratio found for large features in the end-to-end simulations ( $\ln \rho > 2.6$ ), and are comparable to evidence ratios found for simulated bubble collisions in the needlet sensitivity region of parameter space. The features with the largest evidence ratios are given in Table I, along with the marginalized constraints on the model parameters. We have performed simulations of collisions with parameters set by the central values in Table I, and find evidence ratios both below and above the values found in the data; for collisions in this range of parameter space, the particular CMB and noise realization affects our ability to claim a detection.

**Discussion:** We have found four features in the WMAP 7-year data (Table I) that are *consistent* with being bubble collisions. Simulations suggest that the combination of this data-set and our algorithm should be sensitive to bubble collision signatures with parameters similar to those obtained for these possible detections. The Bayesian evidence ratios favouring the bubble collision hypothesis are systematically larger than expected from false detections as calibrated using a bubble collision-free end-to-end simulation of the WMAP experiment. Without the corroborating evidence of a circular temperature discontinuity, we cannot claim a definitive detection. However, data from the *Planck* satellite [17], which has a resolution three times better than that of WMAP, with an order of magnitude greater sensitivity, will greatly improve the performance of every step of our analysis pipeline, allowing us to cross-check and improve upon these results.

Azimuthally symmetric temperature modulations are not unique to bubble collisions; thus it is important to determine if alternative models better fit the data. The automated nature of our pipeline ensures that such comparisons are not based on *a posteriori* choices, and we will apply our algorithm to various models using *Planck* data in future work. As we describe in a companion paper, the conclusive non-detection of a bubble collision can be used to place stringent limits on theories giving rise to eternal inflation; however, if a bubble collision is verified by future data, then we will gain an insight not only into

our own universe but a multiverse beyond.

We are very grateful to Eiichiro Komatsu and the WMAP Science Team for supplying the end-to-end WMAP simulations used in our null tests. SMF is supported by the Perren Fund. HVP is supported by Marie Curie grant MIRG-CT-2007-203314 from the European Commission, and by STFC and the Leverhulme Trust. MCJ and HVP thank the Aspen Center for Physics, where this project was initiated, for hospitality. We acknowledge use of the HEALPix and Multinest packages and the Legacy Archive for Microwave Background Data Analysis (LAMBDA). Support for LAMBDA is provided by the NASA Office of Space Science.

- 
- [1] A. Aguirre, (2007), arXiv:0712.0571 [hep-th].
  - [2] A. Aguirre, M. C. Johnson, and A. Shomer, Phys. Rev. **D76**, 063509 (2007), arXiv:0704.3473 [hep-th].
  - [3] N. Jarosik *et al.*, (2010), arXiv:1001.4744 [astro-ph.CO].
  - [4] A. Aguirre and M. C. Johnson, (2009), arXiv:0908.4105 [hep-th].
  - [5] S. Chang, M. Kleban, and T. S. Levi, JCAP **0904**, 025 (2009), arXiv:0810.5128 [hep-th].
  - [6] C. L. Bennett *et al.*, (2010), arXiv:1001.4758 [astro-ph.CO].
  - [7] D. Marinucci *et al.*, (2007), arXiv:0707.0844 [astro-ph].
  - [8] K. M. Gorski *et al.*, Astrophys. J. **622**, 759 (2005), arXiv:astro-ph/0409513.
  - [9] S. Scodeller *et al.*, (2010), arXiv:1004.5576 [astro-ph.CO].
  - [10] A. de Oliveira-Costa and M. Tegmark, Phys. Rev. **D74**, 023005 (2006), arXiv:astro-ph/0603369.
  - [11] J. Canny, IEEE Trans. Pattern Anal. Mach. Intell. **8**, 679 (1986).
  - [12] C. Kimme, D. Ballard, and J. Sklansky, Commun. ACM **18**, 120 (1975).
  - [13] D. S. Sivia and J. Skilling, *Data Analysis: A Bayesian Tutorial* (Oxford University Press, Oxford, UK, 2006).
  - [14] F. Feroz, M. P. Hobson, and M. Bridges, (2008), arXiv:0809.3437 [astro-ph].
  - [15] M. Cruz, E. Martinez-Gonzalez, P. Vielva, and L. Cayon, Mon. Not. Roy. Astron. Soc. **356**, 29 (2005), arXiv:astro-ph/0405341.
  - [16] D. Pietrobon *et al.*, Phys. Rev. **D78**, 103504 (2008), arXiv:0809.0010 [astro-ph].
  - [17] J. A. Tauber, N. Mandolesi, J. Puget, *et al.*, A&A **520**, A1+ (2010).

$\ln \rho$	$z_0$	$z_{\text{crit}}$	$\theta_{\text{crit}}$	$l_0$	$b_0$
$4.9 \pm 0.2$	$-5.4_{-1.3}^{+1.2} \times 10^{-5}$	$1.0_{-10}^{+10} \times 10^{-6}$	$5.7_{-0.3}^{+0.3}$	$207.3_{-0.3}^{+0.4}$	$-57.0_{-0.2}^{+0.3}$
$5.1 \pm 0.2$	$5.4_{-1.1}^{+1.1} \times 10^{-5}$	$3.3_{-50}^{+50} \times 10^{-7}$	$6.6_{-0.5}^{+0.6}$	$320.7_{-0.5}^{+0.5}$	$-32.7_{-0.4}^{+0.4}$
$4.0 \pm 0.1$	$-5.6_{-1.4}^{+1.4} \times 10^{-5}$	$2.9_{-60}^{+60} \times 10^{-7}$	$3.9_{-0.7}^{+1.0}$	$187.5_{-0.4}^{+0.4}$	$-79.0_{-0.4}^{+0.3}$
$7.0 \pm 0.2$	$-6.3_{-1.3}^{+1.3} \times 10^{-5}$	$7.5_{-7}^{+7} \times 10^{-6}$	$4.5_{-0.3}^{+0.2}$	$268.7_{-0.3}^{+0.3}$	$-77.3_{-0.3}^{+0.2}$

TABLE I. Parameters of the possible bubble collisions detected in the WMAP 7-year data. The reconstructed collision center  $(l_0, b_0)$  is reported in Galactic coordinates. The first entry in this table is the Cold Spot [15]; the second corresponds to a feature identified in Ref. [16].